Supplement of Atmos. Chem. Phys., 21, 357–392, 2021
https://doi.org/10.5194/acp-21-357-2021-supplement

Supplement of

Insights into the aging of biomass burning aerosol from satellite observations and 3D atmospheric modeling: evolution of the aerosol optical properties in Siberian wildfire plumes

Igor B. Konovalov et al.

Correspondence to: Igor B. Konovalov (konov@ipfran.ru)

S1. A note on the differences between the analysis method used in this study and by Konovalov et al. (2017)

While the analysis procedure developed in this study (see Sect. 2.1) is similar to that used by Konovalov et al. (2017), there are also notable differences between these procedures. A major distinctive feature of the analysis in Konovalov et al. (2017) is splitting the available data into several bins, each of which covered a fixed range of photochemical ages. Consequently, the results of the analysis depended on the chosen width of the photochemical age bin. In this study, we avoided the intrinsic uncertainty associated with a choice of the photochemical age bin width by fitting all the available data at once with a "universal approximator". The optimal approximation still depends on the structural parameter (*N*), but the choice of the optimal parameter value in this study is rather straightforward and objective, as described in Sect. 2.1. Overall, we believe that the analysis procedure used in the framework of this study is superior to the procedure employed in the previous study, enabling more reliable detection of the aging changes in the BB aerosol properties.

S2. Box model simulations

Here we present the simulations performed with a microphysical dynamic (box) model of organic aerosol. The model is described in detail in Konovalov et al. (2019), where five different VBS schemes were used to simulate the BB OA evolution in an isolated plume under the prescribed ambient conditions. In the present study, box model simulations were performed using our simplified adaptive VBS scheme as well as the original 1.5-dimensional (C17) one (Ciarelli et al., 2017) from which our scheme was derived. Air temperature and the initial BB OA mass concentration were chosen to be representative of the conditions of the four "high-temperature" chamber experiments reported by Ciarelli et al. (2017). These experiments were conducted at a temperature of 288.15 K, with the initial BB OA mass concentration varying in the narrow range from 17.55 to 22.63 μg m^{-3}. In our model runs, we set the temperature accordingly at 288.15 K and assumed the fixed value of 19 μg m^{-3} for the initial BB OA mass concentration. Note that the "low-temperature" experiments conducted by Ciarelli et al. (2017) at 263.15 K are not considered here because according to our simulations (see Sect. S4 below), the typical ambient temperature at the locations of the center of mass of the analyzed BB plumes was significantly higher than 263.15 K (ranging from about 280 to 285 K). Dilution and the background OA concentration, which were taken into account in the analysis reported in Konovalov et al. (2019), were disregarded in the simulations presented here, which are intended to replicate the conditions of chamber experiments. The parameters of our simplified VBS scheme (the reaction rates, enthalpies of evaporation, stoichiometric coefficients, and the ratio of the initial mass concentration of NTVOCs to the sum of the initial mass concentrations of the POA species) were chosen to be the same as those reported in Sect. 2.4 and Tables 1 and 2. As explained in Sects. 2.4 and 2.6, a few parameters (specifically those defining HV-SOA and LV-SOA yields, the product yields from the oxidation reactions of MV-SOA and LV-SOA, and the emission ratio of mass concentration of NTVOCs to the sum of mass concentrations of the POA species) were optimized in this study using satellite observations. The parameters of the C17 scheme were adopted from Ciarelli et al. (2017, see Table 1 therein). Note that these parameter values were partly constrained by data from both the low-temperature and high-temperature experiments (see Ciarelli et al., 2017 for details). The model runs were performed for a period of 110 hours. This period corresponds to the estimated maximum duration of the exposure of smoke plumes to sunlight in the analyzed region and period (see Sect 3.2). The OH concentration was fixed at 5×10^6 molec cm^{-3}.

The results of our simulations are presented in Fig. S1. Specifically, the figure shows the time series of the total BB OA mass concentration and also illustrates changes in the fractional composition of BB OA. The calculations can be compared to measurements of the BB OA mass concentrations at the high-temperature experiments. The BB OA concentration initially enhances more rapidly in the simulation with our scheme (Fig. S1a) than in the simulation with the original scheme (Fig. S1b). As a result, the BB OA concentration predicted by our scheme after about 10 hours of evolution is about 40 % larger than the corresponding concentration predicted by the original C17 scheme. It is also about 15% larger than the maximum concentration obtained in the chamber experiments. However, it should be noted that these particular experiments are not representative of the wide range of burning conditions and large variety of fuels in the Siberian forest. Moreover, there was significant variability in BB OA concentrations even under the controlled conditions of the chamber experiments (Fig. S1). Taking these observations into account, we consider the comparison presented in Fig. S1a as additional evidence that the simulations of the BB OA evolutions with our simplified scheme are sufficiently reasonable. A comparison of the results obtained with the simplified and original schemes (cf. Fig. S1a and Fig. S1b) reveals that the simulations are qualitatively different. Indeed, while the original scheme demonstrates a monotonic saturating increase of BB OA concentration, the simplified scheme yields a non-monotonic behavior of BB OA concentration (a rapid increase followed by a gradual decrease due to fragmentation of SOA). These two types of behavior of BB OA were earlier identified and discussed in Konovalov et al. (2019). However, the available chamber experiments, which are representative of only relatively small OH exposures, do not allow us to exclude any of these types of behavior of BB OA aerosol.

Since the definitions of surrogate organic species in our VBS scheme and C17 schemes are considerably different, a direct comparison of the simulated compositions of OA is not feasible. Nonetheless, the comparison of Fig. S1a and S1b reveals some obvious similarities between the simulations with the two schemes. In particular, there is a decreasing trend of POA in the both simulations; there is also a steep increase in the concentration of the secondary compounds in the medium volatility range during the first several hours and eventual disappearance of these compounds. In both simulations, the low –volatility components ($C^*<10^0$ μg m^{-3}) provide predominant contributions to the BB OA composition at the end of the evolution period. Overall, this comparison indicates that the BB OA behavior predicted by our scheme is not strikingly different from that predicted by the C17 scheme and is physically reasonable. The major differences are associated with the dynamics of the medium-volatility components.

S3. Time series of AOD and CO data from the ancillary data set

Figure S3 shows the time series of AOD retrieved from the MODIS measurements and simulated with CHIMERE for all the three main modeling scenarios considered in this study. The time series for the MODIS AOD observations and the simulations for “bb_vbs’ scenario correspond to the spatial distributions shown in Fig. 2. Similar time series for the CO columns corresponding to the spatial distributions shown in Fig. S2 are presented in Fig. S4. The time series are shown separately for the source and receptor regions. The differences between the simulations performed with and without fire emissions are indicative of the BB fraction of AOD or CO columns. Note that these time series represent the ancillary dataset (see Sect. 2.5), which does not include the OMI observations. Both the observations and simulations exhibit strong AOD and CO enhancements, which (according to our simulations) were caused predominantly by fire emissions in Siberia. In the source region, the fires strongly affected AOD and CO from the end of June until the end of July, and the enhancements were particularly strong during the analysis period (from 15 to 31 July). In the receptor region, considerable AOD and CO enhancements were observed only in the period from 18 to 31 July. These enhancements caused by the major outflow of BB plumes from Siberia are in striking contrast with much lower values of both characteristics outside of the analysis period.

The simulations taking fire emissions into account are in good agreement with the observations, with the correlation coefficient typically exceeding 0.85. There are, however, some noticeable differences between the simulations for the “bb_vbs’ and ‘bb_stn’ scenarios. In particular, while the simulations for the ‘bb_vbs’ scenario slightly (by ~7 % percent on average) underestimate AOD in the source region, they are in nearly perfect agreement (again on average) with the observations in the receptor region. In contrast, the “standard” simulations agree with the observations in the source regions but are biased high (by ~18 %) in the receptor region. Note that the fire emissions used in our simulations were optimized (see Sect. 2.6) using the main dataset, which is consistent with the OMI AAOD observations and contains much fewer data points than the ancillary dataset (which includes AOD and CO observations irrespective of the availability of the corresponding AAOD retrievals) presented in Figs. 2, and S2-S4. This explains some noticeable differences between the average AOD or CO values from the observations and simulations in the source region.

S4. Evolution of ambient parameters

Here we consider the behavior of several characteristics that can affect the gas-particle partitioning and oxidation processes in the BB plumes as well as the estimates of the AAOD and AOD enhancement ratios. To this end, Figure S6 presents the simulated trends in several quantities, including ambient temperature and relative humidity (Fig. S6a), the height of the BB plume mass center and OH concentration (Fig. S6b), and total BB OA concentration (Fig. S6c). All the characteristics are calculated as the weighted average over the vertical profile of the plume, with BB aerosol mass concentration being used as weights. Additionally, Fig. S6c shows the trend in the normalized ratio of the BB tracer’s AAOD (τ_{abs}^{t}) involved in Eq. (1) to the column amount of the inert gaseous tracer of BB OA emissions, T_1 (see Sect. 2.3). This ratio characterizes the changes in AAOD due to dry deposition, wet scavenging, and coagulation of particles.

It can be seen that the average temperature fluctuates around 10° C and does not exhibit any considerable trend. The relative humidity (RH) is typically very low, with the average values being below 50% for the BB aerosol aged less than 70 h. The BB plume height initially increases from about 1.5 to 1.8 km during the initial 30 h of the daytime evolution and then slightly decreases. There is also only a slight downward trend in the OH concentration during the initial period. The regular changes in all these characteristics are overall rather small and could hardly induce the significant trends in AAOD and AOD that are identified above. In contrast, rather significant changes occur in the simulated average concentration of BB OA, which drops from 62 to 13 μg m^{-3} (see Fig S6c). This is an expected effect of the dilution of BB plumes. The dilution is associated with increasing the equilibrium concentration of SVOCs, favoring evaporation of particulate organic material and more rapid losses of SVOCs as a result of gas-phase fragmentation reactions. These processes are driving the decrease of both AAOD and AOD after t_e of ~30 h (see Fig 5a, b).

Figure S8c also indicates that the basic aerosol processes included in the “tracer” simulation could not significantly affect the BB aerosol evolution. As could be expected, the ratio of AAOD computed for the inert aerosol tracer (τ_{abs}^{t}) to the column mass concentration, [T1], of the inert gaseous tracer decreases with time, apparently mostly as a result of dry deposition (as according to our meteorological simulations, there were almost no precipitation events in the region and period considered), but coagulation could also contribute to this trend (Sakamoto et al., 2015). Virtually the same dependence, which is not shown, is found for τ_{ext}^{t}. The rate of the decrease of the τ_{abs}^{t}-to-[T1] ratio is much slower than the expected rate of the loss of BB BC from the lower atmosphere: indeed, the atmospheric lifetime of BC in Siberia was estimated to be only about 5 days under typical conditions (Paris at al., 2009). However, this lifetime is partly determined by wet deposition, and it also should be taken into account that τ_{abs}^{t} at 388 nm is mostly determined by relatively small and thus long-lived particles in the accumulation mode, whereas the total BC concentration can be dominated by larger particles. This consideration implies, in particular, that the appearance of the decreasing parts of the EnR trends derived from the observed values of AAOD and AOD (see Fig. 5a, b) cannot be due to underestimation of dry deposition of BB aerosol in our simulations of the BB aerosol tracers. Note again that coagulation can also contribute to the changes of τ_{abs}^{t} and τ_{ext}^{t} due to aging by modulating the size distribution, but the corresponding effects have not been isolated in this study.

S5. Simulation results for the ‘bb_poa’ simulation scenario

The ‘bb_poa’ simulation test scenario that was introduced in Sect. 2.3 and discussed in Sect. 3.3 addresses a hypothetical situation where the organic components of BB aerosol are not affected by any oxidation reactions. For this scenario, we also postulated that the POA species are hygroscopic instead of being hydrophobic as in the bb_vbs scenario to compensate for the water uptake by the SOA species. The simulations were performed using the same model configuration as for the ‘bb_vbs’ scenario except that all the reaction rates reported in Table 2 were set to zero, the hygroscopicity parameter κ_{org} for both LV-POA and MV-POA was assumed to be 0.2, and the POA emissions were increased by a factor of 4.3. Using the simulated concentrations for this scenario, we also performed an additional calculation with the OPTSIM module for a test case in which the contribution of water to the BB aerosol composition was neglected. The main simulation results are presented in Fig. S8.

According to these results, EnRs for both AAOD and AOD (see Fig. S8a, b) demonstrate monotonous decreasing dependencies, in a striking contrast to the non-monotonous dependencies obtained from satellite observations (cf. with Fig. 5a, b) and simulations for the ‘bb_vbs’ scenario (cf. with Fig. 7a, b). The decrease in EnR_{abs} is substantial (~50 %), while that in EnR_{ext} is small (~10 %). Consistently with the monotonous changes in AOD and AAOD, SSA gradually increases (Fig. S8c), instead of demonstrating a hyperbolic (saturable) dependence on the BB aerosol photochemical age as in our analysis of the satellite data (see Fig. 5c). The corresponding values of the mass absorption and scattering efficiencies (α_a and α_s, respectively) indicate (see Fig S8d) that the decrease in α_a (which is expected to occur due to the limited lifetime of BrC in the primary aerosol, see Sect. 2.4) is the main factor responsible for the strong decrease in EnR for AAOD. The main process underlying the decrease in EnR for AOD is apparently the evaporation of MV-POA, since in contrast to α_a, α_s increases as a result of the BB evolution (by 44 %). The increase in α_s can be due to changes in the particle size distribution upon the evaporation of MV-POA, as well as due to an increase in the water uptake as a result of the rise in RH (see Fig. S6a). The test OPTSIM calculation, in which the contribution of water to BB aerosol was disregarded and α_s is found to increase by 27 % (see a brown line in Fig. S8d), confirms that the increase in the water uptake is important but not the major factor underlying changes in α_s. It may be noteworthy that the initial – for the period considered – value of α_s in the ‘bb_poa’ scenario (6.4 m^2 g^{-1}) is found to be larger than that in the ‘bb_vbs’ scenario (4.0 m^2 g^{-1}, see Fig. 9). A more detailed examination of the simulation data reveals that this difference is associated with the differences in the corresponding particle volume size distributions. Specifically, the ‘bb_vbs’ simulation allocates a much larger fraction of the particle mass to the particles with diameters around 100 nm or less, which have a relatively small scattering efficiency, than the ‘bb_poa’ simulation. In the ‘bb_vbs’ simulation, these particles consist predominantly of the SOA species and are, therefore, formed as a result of oxidation of NTVOC and POA. Further SOA formation results in the growth of these particles, pushing the size distribution toward larger values as illustrated in Fig. S7. The difference between values of the absorption efficiency for the ‘bb_vbs’ and ‘bb_poa’ scenarios is determined by the difference in the absorptive properties of the POA and SOA species and is not of interest in the context of this study.

Overall, the simulation results presented in Fig. S8 indicate that the evaporation of POA and the water uptake by BB aerosol particles cannot explain a prominent increase in EnR for AOD, which is found both in the analysis of satellite data and in our simulations for the base case (‘bb_vbs’) scenario. Accordingly, the simulation for the ‘bb_poa’ scenario confirms that the strong increase in AOD is primarily a result of oxidation processes leading to the SOA formation. The analysis presented here may also have a wider implication when considered together with the OC emission estimates discussed in Sect. 2.6. Specifically, it provides further evidence that if a given model strongly underestimates AOD (with respect to satellite observations), this fact does necessarily mean that the underestimation is due to a negative bias in BB emission inventory data. Instead, it may be due to insufficiently strong SOA formation in the model. The proposed joint analysis of satellite and model data allows distinguishing between the two possible reasons for the underestimation of AOD by the model. If AOD is underestimated as a result of missing SOA formation processes, the adjustment of the POA emissions in the model would not enable it to reproduce the major features of the retrieved evolution of the BB aerosol optical properties, as demonstrated in our analysis presented in this section.

S6. The relative contribution of BC, lensing effect, and BrC to the BB aerosol absorption

Figure S9 shows the fractional contributions of BC, lensing effect, and BrC to absorption at 388 nm as a function of BB aerosol photochemical age according to our simulations for the ‘bb_vbs’ scenario with different assumptions examined in Fig. 10. These computations are carried out using two approaches. First (see Fig. S9a), we computed the absorption determined by BC and the OA lensing by setting the imaginary refractive indexes for POA and SOA to zero. The difference between the “base case” simulation (Fig. 7a) and the test case simulation with non-absorbing OA (Fig. 10c) is regarded as a contribution of BrC to absorption. Second (see Fig. S9b), we computed the absorption determined only by BrC (Fig. 10b) and regarded the difference between the “base case” simulation and this test case simulation as a contribution of BC (with the OA lensing) to absorption. These approaches are not expected to yield identical results because of the “sunglasses effect” of BrC, that is, the blocking effect of an absorbing coating on the absorption associated with the BC core (Luo et al., 2018). An optically thick BrC shell could account for virtually all the absorption according to the second approach, irrespective of the BC content. However, our absorption estimates for the second approach turned out to be only insignificantly larger than those for the first approach, thereby indicating that the sunglasses effect does not play a major role in our situation.

According to our computations (Fig. S9a), “pure” BC accounts on average (over the study region and analysis period) for only 31% of the total absorption. The BC contribution is the smallest (28 %) at t_e of 17 h and largest (54 %) at the end of the evolution period. The lensing effect (see Fig. 10c) leads to an enhancement of the BC absorption by 80 % on average, contributing about 20 % to the absorption. Finally, compared to the sensitivity case with non-absorbing OA, the base case absorption that includes the contribution of BrC is, on average, 78 % larger. According to Fig. S9b, BrC contributes about 50 % to the BB aerosol absorption at the beginning of the evolution period considered, but less than 15% at the end of the period. Based on our additional computations, the percentage contribution of BrC to absorption BrC by POA in fresh BB aerosol (which is not covered by our analysis) is also about 50%, which is within the broad range of values (21-80%) reported by Pokhrel et al. (2017) for aerosol originating from combustion of samples of pine and black spruce trees. Accordingly, we estimate that the BrC contribution to the BB aerosol absorption is reduced by more than a factor of 3 after about 100 hours of daytime evolution. Hence, our simulations suggest that consistent with observational findings (Forrister et al., 2015; Selimovic et al., 2019), BrC absorption is strongly decreasing when BB aerosol is exposed to atmospheric processing under daytime conditions. On the other hand, consistent with the analysis of the AERONET data by Wang et al. (2016), our results indicate that a sizeable BrC fraction is resistant to both photooxidation and photobleaching. According to our analysis, this fraction, which is likely associated with high-molecular-weight chromophores (Di Lorenzo et al., 2017, Wong et al., 2017, Fleming et al., 2020), remains a significant contributor to the absorptive properties of BB aerosol even after several days of atmospheric aging.

S7. Sensitivity analysis

As noted in Sect. 2.2, one of the important features of the OMAERUV data products is that the AAOD and SSA retrievals are dependent on the BB plume height, which needs to be assumed a priori and can be a source of systematic uncertainty in the results of our analysis. While the base case results presented above are obtained using the BB plume heights predicted by our model independently for each grid cell and hour, we also tested the ‘final’ OMAERUV retrievals based on the monthly aerosol layer height climatology derived from CALIOP measurements (Torres et al., 2013). Assuming a constant aerosol layer height for a whole month is effectively equivalent to disregarding possible dependencies of this parameter on the intensity of fires and plume age and could, therefore, result in some systematic errors in our analysis. On the other hand, the emission injection heights estimates involved in our simulations are likely affected by the uncertainty dominated by random errors associated with the corresponding parameterization (Sofiev et al., 2012). Accordingly, we consider the differences between the BB aerosol absorption trends inferred from the different subsets of the OMAERUV data as an indicator of the robustness of the results of our analysis with respect to both possible systematic and random uncertainties in the aerosol layer height. We find that the results obtained with the ‘final’ retrievals of both AAOD and SSA (see Fig. S10a, b) are only slightly different from those for the base case (see Fig. 5a, d, respectively). Specifically, the amplitude of the variation of the AAOD trend is insignificantly smaller, and the SSA values are slightly higher in the test case than in the base case.

One more potential source of systematic uncertainty in our analysis is associated with the use of the IASI CO data to correct possible transport errors by applying the correction factor f_c (see Sect. 2.1 and Eqs. 2 and 3). This uncertainty may appear for two main reasons. First, the IASI CO columns are likely to be underestimated close to emissions (Turquety et al., 2009). Second, our estimates of f_c can be affected by uncertainties in the background part of the CO columns. In the situation addressed in this study, a negative bias in the IASI CO columns in the source region – since the CO emissions from fires were fitted to the IASI observations in the source region – would likely result in underestimation of CO columns in our simulations for the receptor region. However, our analysis does not reveal any significant biases in our simulations (see Figs. 4f and S4). The potential bias in the simulated data could hardly be compensated by the transport errors because the data are averaged over many grid cells representing the source and receptor regions. Thus we do not see any evidence of the impact of potential biases in the IASI CO columns on our estimates of the correction factors f_c. The effects of potential uncertainties in the background CO columns on our estimates are more difficult to evaluate, particularly because these uncertainties can vary in both space and time. Underestimation of the background CO would result in overestimation of f_c, making the downward trends of $\mathrm{EnR_{abs}}$ and $\mathrm{EnR_{ext}}$ stronger, and vice versa. However, the de-biasing procedure used in our analysis (see Sect. 2.5) is expected to ensure that such effects are not considerable overall. Indeed, we find that the de-biased CO columns simulated without fire emissions are in good agreement with the IASI CO columns both in the source and receptor regions on the days when the contribution of fire emissions was negligible (see Fig. S4). To test the overall impact of the CO data on the derived trends in $\mathrm{EnR_{abs}}$ and $\mathrm{EnR_{ext}}$, we repeated the analysis of the AAOD and AOD data with f_c equal to 1. The results of the test (see Fig. S11) are qualitatively (although not necessarily quantitatively) similar to those for the base case (see Fig. 5a, b). We regard these sensitivity test results as strong evidence that the main features of the inferred trends in $\mathrm{EnR_{abs}}$ and $\mathrm{EnR_{ext}}$ are not an artifact of the proposed correction of the aerosol tracers and possible uncertainties associated with it, and are not significantly affected by uncertainties in the observations and simulations of the CO columns.

Finally, we examined the sensitivity of the inferred evolution of $\mathrm{EnR_{abs}}$ and $\mathrm{EnR_{ext}}$ to the assumptions about the background AAOD and AOD values involved in Eq. (1). It may be useful first to recall that we assumed the background AAOD values to be negligible when compared to the OMI AAOD retrievals, mainly because it is not known how the background part can be accounted for in the OMI AAOD retrievals for the “biomass burning” type of aerosol (see Sect. 2.3). Nonetheless, we roughly estimated to which degree our estimates could change if the OMI AAOD retrievals included an additive “background” part. The OMAERUV algorithm identifies – as noted above – three types of aerosol, but only one (“biomass burning”) type is used in our analysis presented above. To get an idea about the typical magnitude of AAOD at 388 nm under background conditions, we used – in addition to the Level-2 BB aerosol data – the daily Level-3 OMAERUV data which combine all three aerosol types and are available from the Giovanni online application (https://giovanni.gsfc.nasa.gov/giovanni/, last access 11 April 2020) on a 1-by-1-degree grid. According to these data, the mean AAOD in the receptor region in the period from 15 June to 15 July (where and when there was no discernible fire activity) was about 0.018. This value was used as an estimate of τ_{abs}^{bgr} in Eq. (1). Not surprisingly, the resulting approximation (see Fig. S12a) exhibits a stronger downward trend, but the AAOD evolution remained qualitatively the same as in the base case (see Fig. 5a). It should be noted that the Level-3 AAOD data are expected to provide an upper limit for the background AAOD because clean scenes typically dominating in the receptor region cannot be associated with any of the three aerosol types. To examine the sensitivity of $\mathrm{EnR_{ext}}$ to the background values of AOD, we repeated our analysis by assuming that τ_{ext}^{bgr} equals to zero. In this case, the decline of $\mathrm{EnR_{ext}}$ is smaller (see Fig. S12b) than in the base case (see Fig. 5b), but is still statistically significant. Hence, based on the results of the tests involving different assumptions on the background values of AAOD and AOD, we can conclude that (i) the impact of the unknown true background AAOD in Eq. (1) on the results of our analysis of EnR_{abs} is probably small and (ii) the declining part of the estimated trend in EnR_{abs} is not due to any bias in our estimates of τ_{ext}^{bgr} .

Supplementary figures

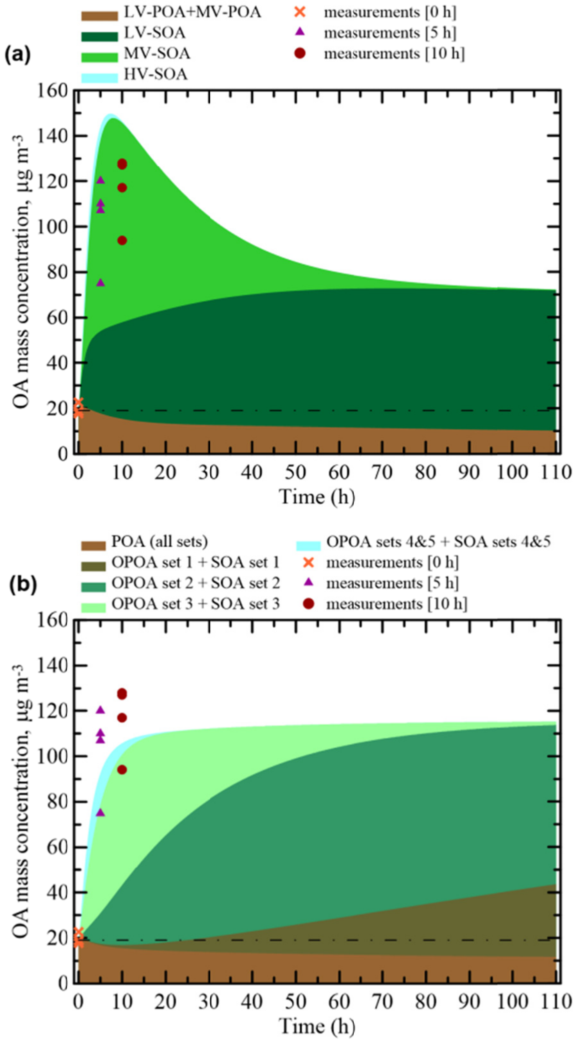

Figure S1. The dynamics of the mass concentration of BB OA and several groups of its components according to the simulations performed with a box model using (a) the simplified VBS parameterization introduced in this paper (see Sect. 2.4) and (b) 1.5-dimensional VBS scheme proposed by Ciarelli et al. (2017). The crosses, triangles, and dots depict the BB OA mass concentration measurements (Ciarelli et al., 2017) originally reported for the OH exposures of 0, 30×10^6, and 50×10^6 molec cm^{-3} h, respectively, and corresponding to 0, 5, and 10 hours of the exposure of BB aerosol to oxidation processes under the assumption that OH concentration equals to 5×10^6 molec cm^{-3}.

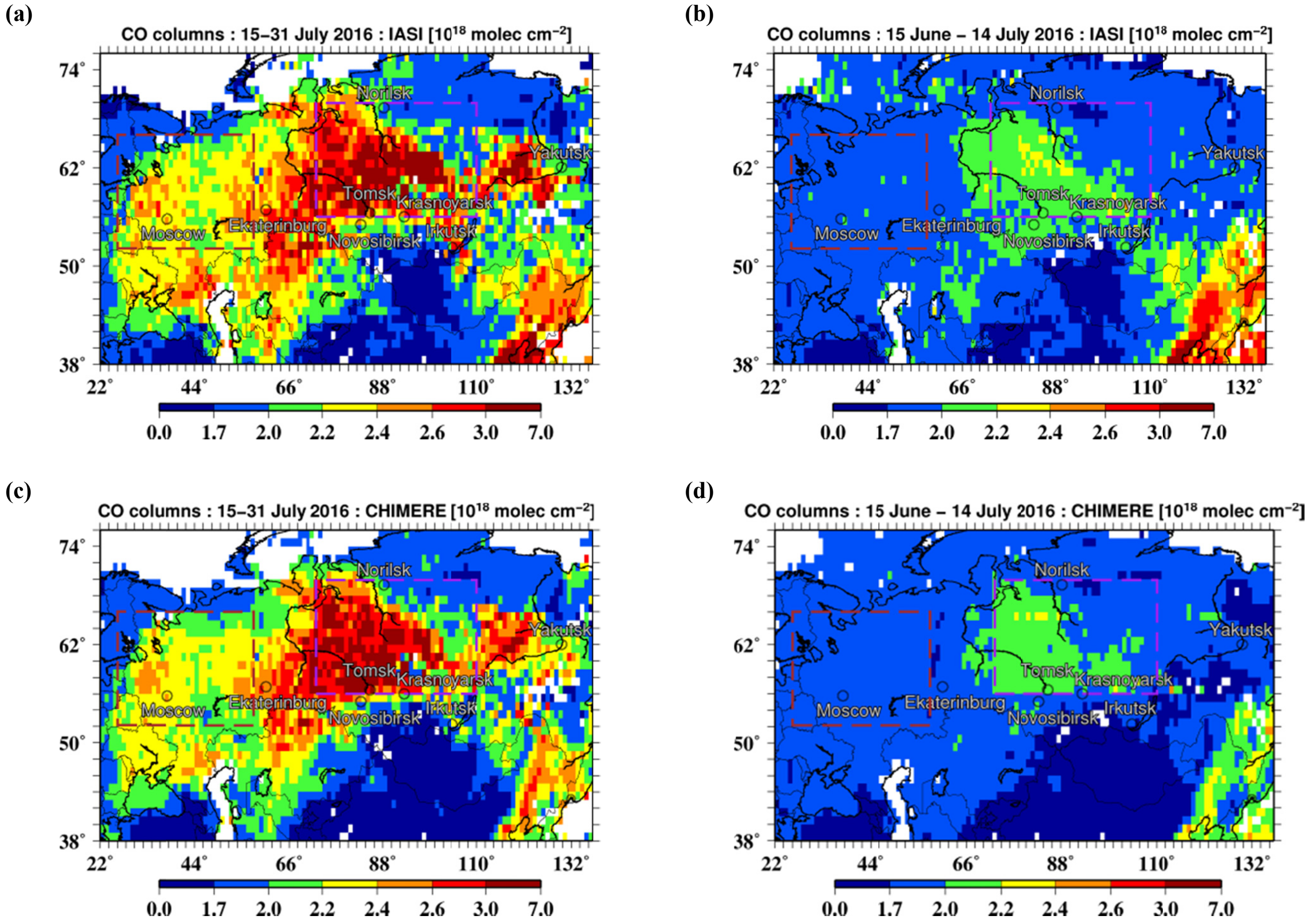

Figure S2. Spatial distributions of temporal averages of CO columns in the periods (a,c) from 15 to 31 July 2016 and (b,d) from 15 June to 14 July 2016 according to (a,b) the IASI observations and (c,d) the combined CHIMERE simulations for the 'bb_vbs' and 'bgr' scenarios. The distributions represent the ancillary sets of CO data that were selected irrespective of the availability of the corresponding AAOD retrievals. The rectangles depict the "source" (purple lines) and "receptor" (dark red lines) regions covering parts of Siberia and (mostly) the European territory of Russia, respectively.

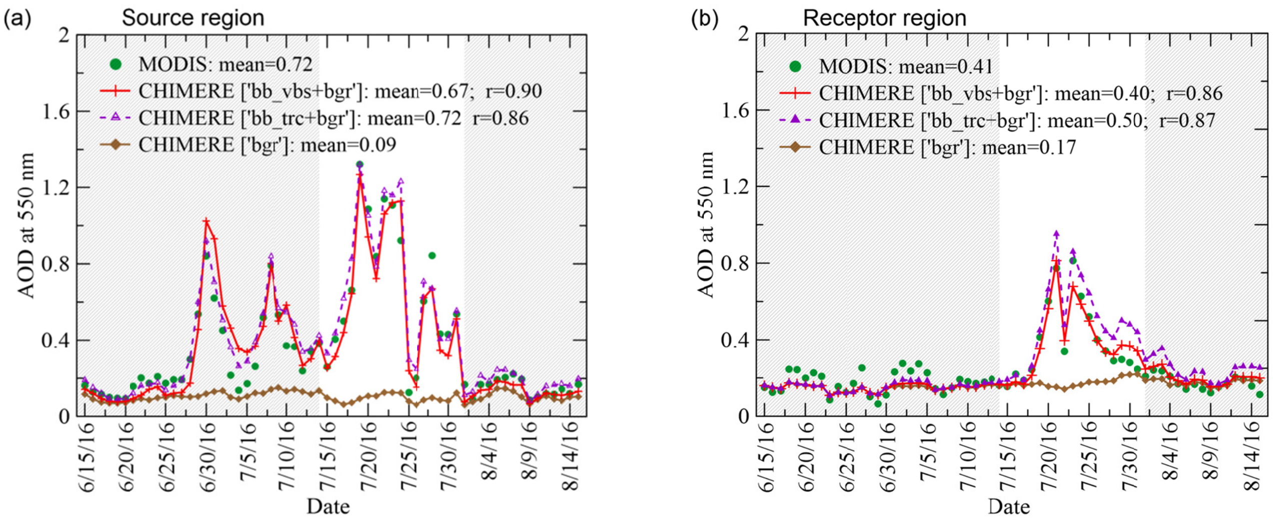

Figure S3. Time series of the daily AOD values averaged over the study region according to the MODIS observations and the CHIMERE simulations under the different model scenarios for the (a) "source" and (b) "receptor" regions indicated in Figs. 2 and S2. Note that the simulations for the 'bgr' (background) scenario are shown after applying the de-biasing procedure (see Sect. 2.5). The shaded areas indicate the days that are outside of the analysis period (15-31 July 2016) in the given study. The mean and correlation coefficient are evaluated for the analysis period.

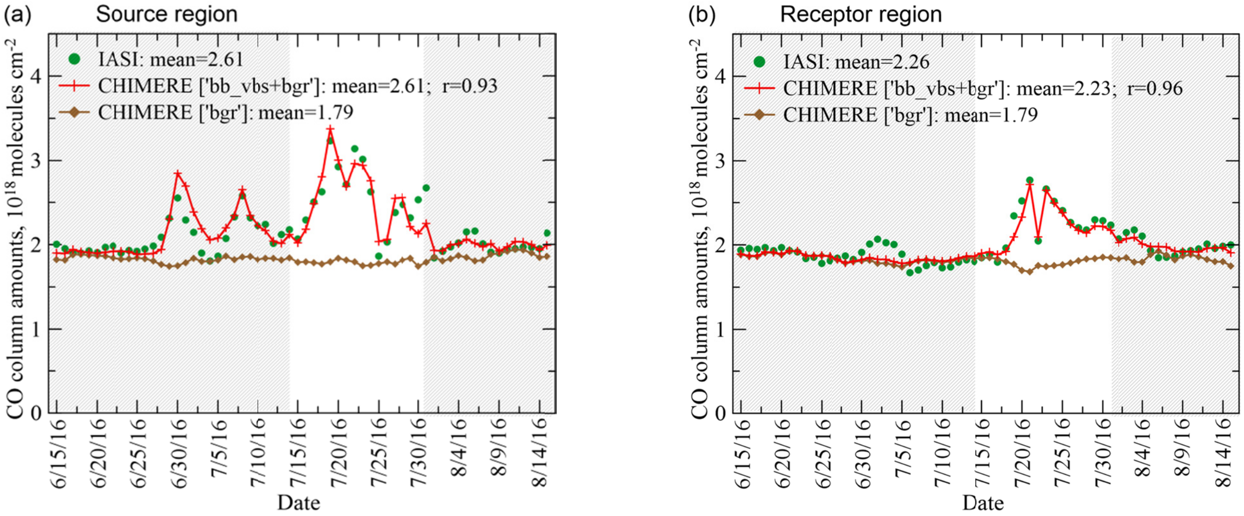

Figure S4. Time series of the daily CO column values averaged over the study region according to the IASI observations and the CHIMERE simulations for the (a) "source" and (b) "receptor" regions. Note that the CO simulations for the 'bb_vbs' and 'bb_trc' scenarios are almost indistinguishable, so only simulations for the 'bb_vbs' scenario (combined with the simulations for the 'bgr' scenario) are shown. Note also that the simulations for the 'bgr' (background scenario) are shown after applying the de-biasing procedure (see Sect. 2.5). The shaded areas indicate the days that are outside of the analysis period (15-31 July 2016) in our study. The mean and correlation coefficient are evaluated for the analysis period.

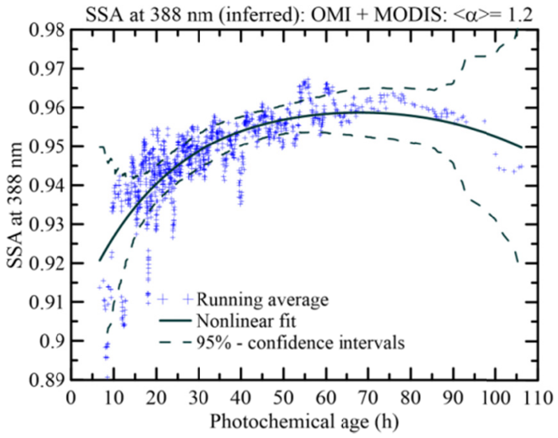

Figure S5. Nonlinear approximation (see Eq. 5) of the dependence of SSA (388 nm) on the photochemical age of BB aerosol. The SSA values were inferred from the OMI AAOD (388 nm) and MODIS AOD (550 nm) observations using the variable extinction Ångström exponent (α) estimates based on the CHIMERE simulations for the 'bb_vbs' scenario.

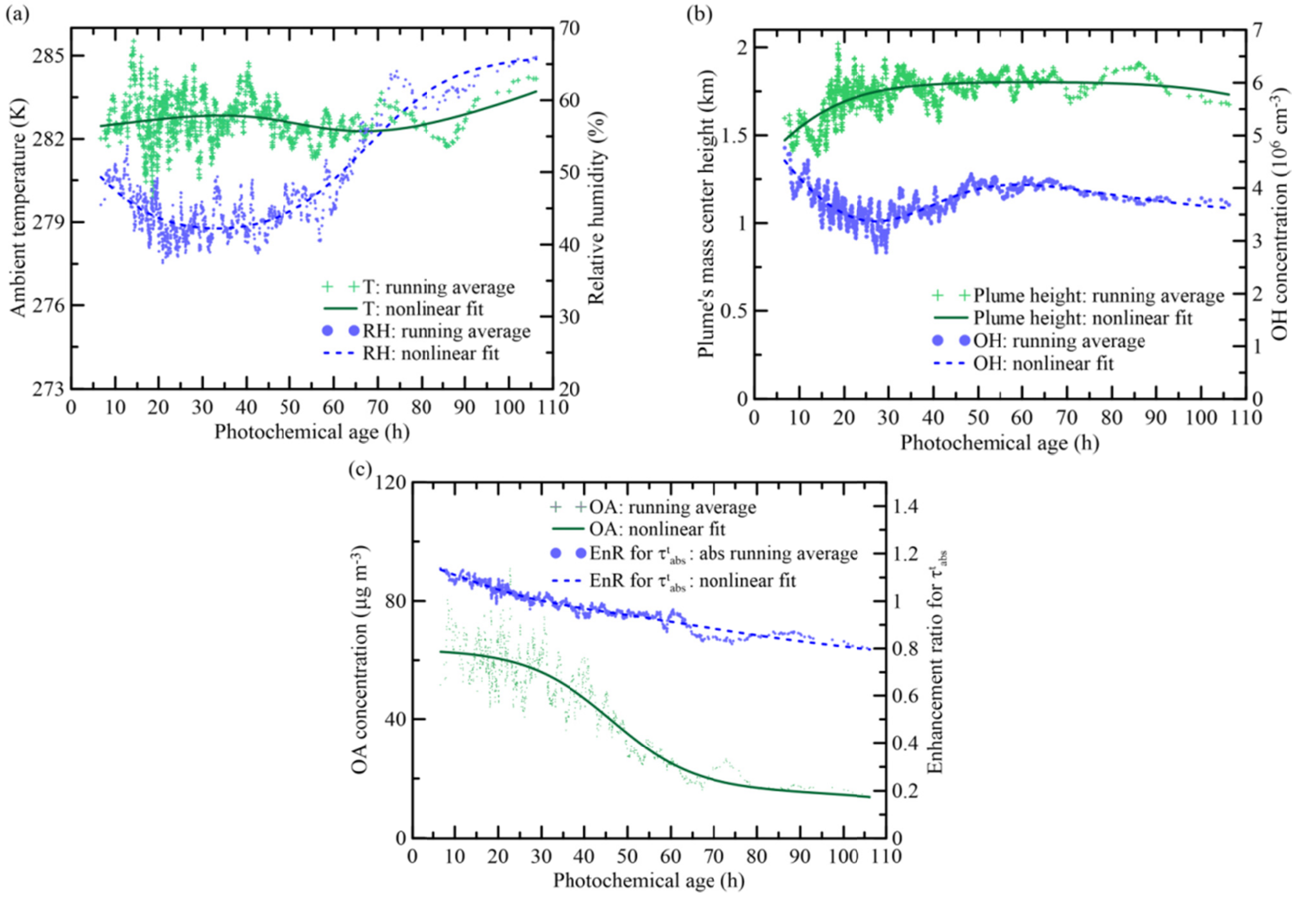

Figure S6. Nonlinear trends in several parameters characterizing the conditions of the atmospheric evolution of BB aerosol in the plumes considered: (a) ambient temperature and relative humidity, (b) the height of the BB plume mass center and OH concentration within a plume. Also shown (c) the trends in total BB OA concentration and the normalized ratio of BB tracer's AAOD (τ_{abs}^{t}) to the column amount of the inert gaseous tracer of BB OA emissions (T_1).

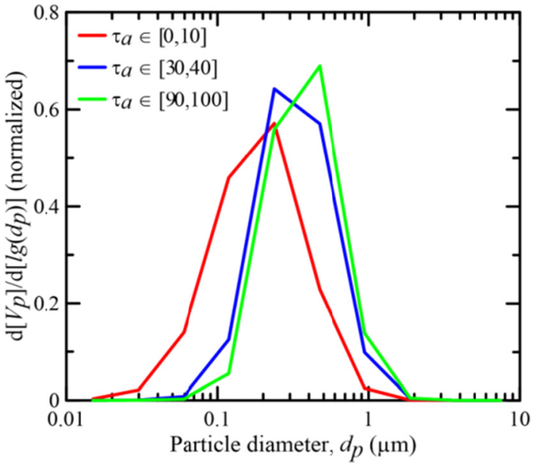

Figure S7. Normalized particle volume size distributions averaged over three intervals – [0,10], [30,40], [90,100] – of the BB aerosol photochemical age (h) according to the simulations for the 'bb_vbs' scenario.

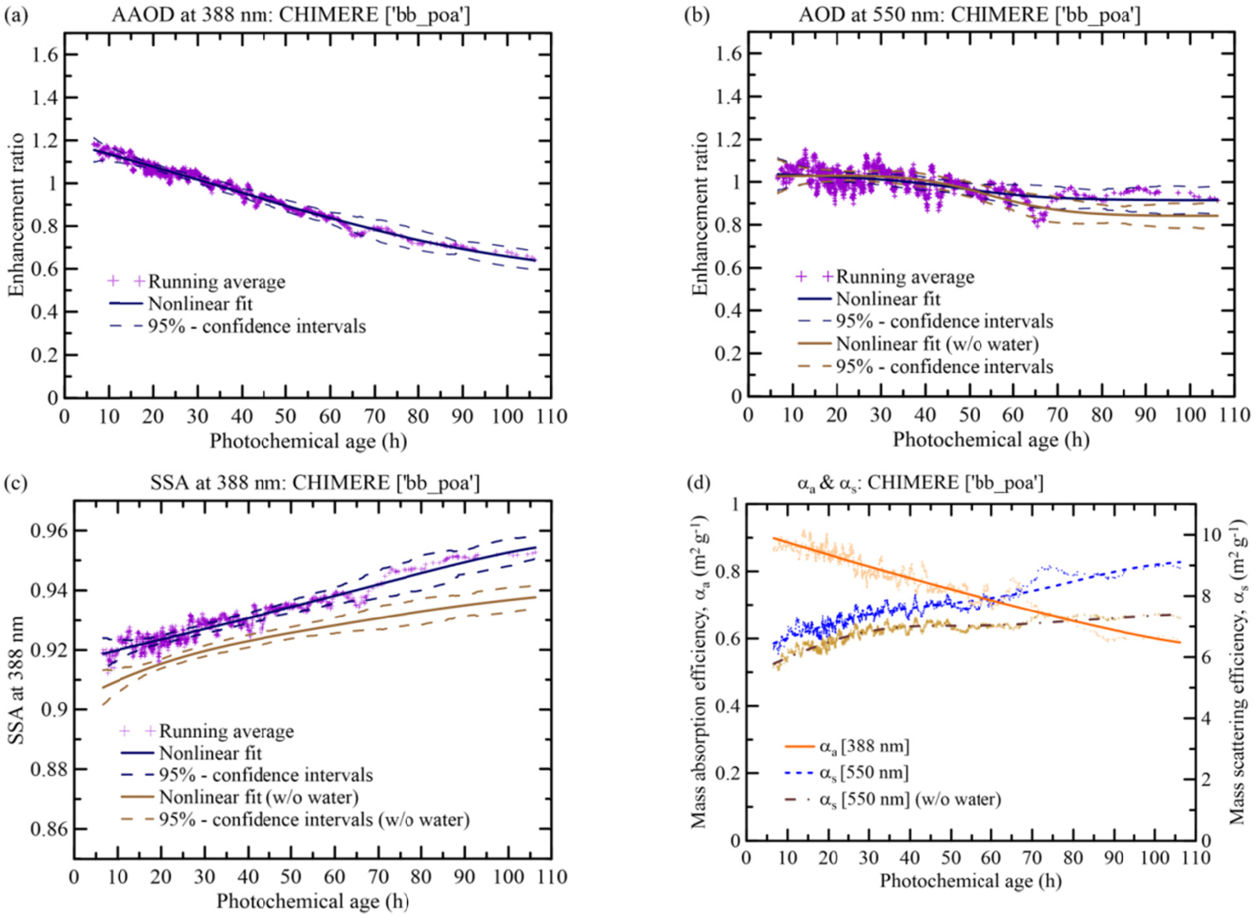

Figure S8. Dependencies of (a, b) EnRs for AAOD (388 nm) and AOD (550 nm) (respectively), (c) SSA (388 nm), and (d) mass absorption and scattering efficiencies (388 nm and 550 nm, respectively) on the photochemical age of BB aerosol according to the simulation for 'bb_poa' scenario. Also shown (brown lines in panels b-d) the corresponding dependencies of EnRs for AOD, SSA and the mass scattering efficiency according to the OPTSIM calculations with the neglected contribution of water to the particle composition; similar dependencies of the AAOD and the mass absorption efficiency are not shown as they visually merge with the dependencies shown by blue and orange lines in panels (a) and (d), respectively.

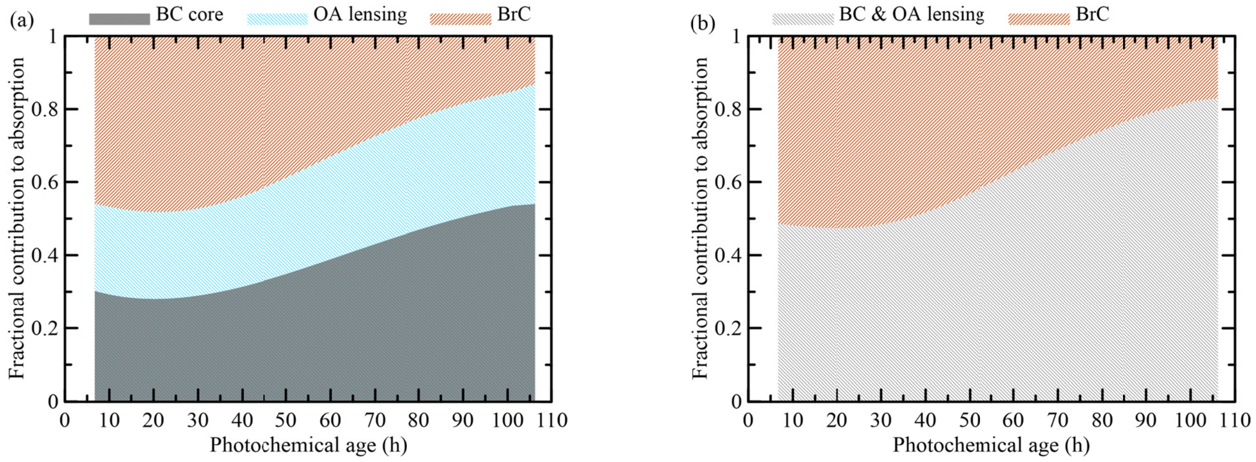

Figure S9. Fractional contributions of BC, lensing effect and BrC to absorption at 388 nm as a function of BB aerosol photochemical age according to the simulations for the 'bb_vbs' scenario with the CHIMERE CTM and OPTSIM software. The contributions shown in panels (a) and (b) are evaluated using the first and second approaches described in Sect. S6.

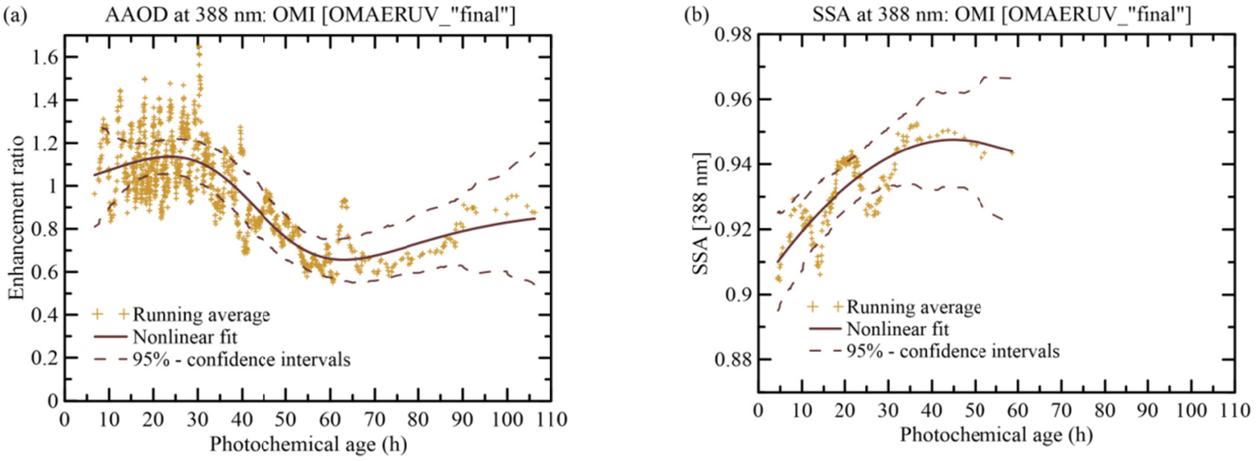

Figure S10. Nonlinear approximations (see Eq. 5) of the dependencies of EnRs for (a) AAOD (388 nm) and (b) SSA (388 nm) on the photochemical age of BB aerosol. The dependencies are similar to those shown in Fig. 5a and 5d except that they are obtained using the "final" OMAERUV data product.

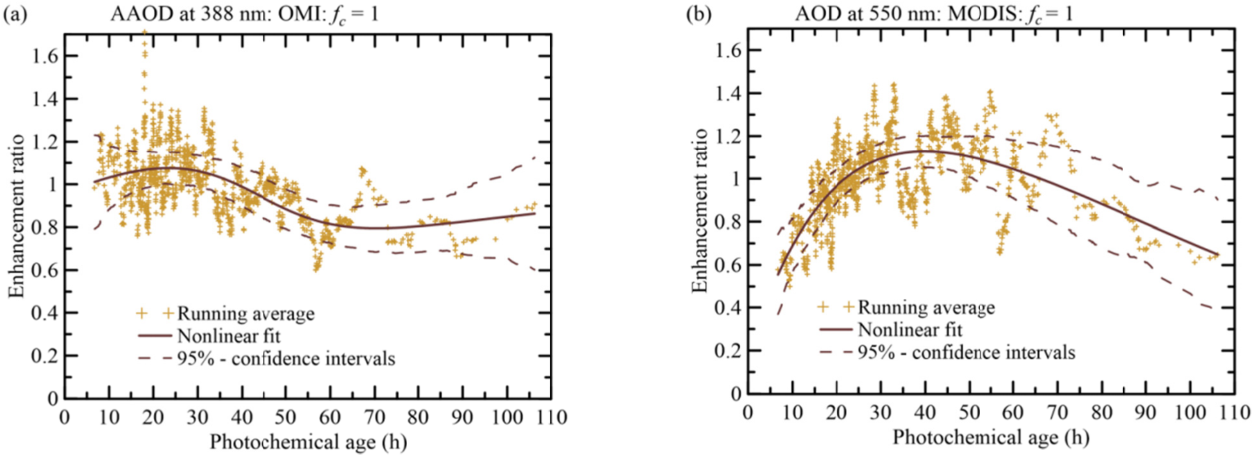

Figure S11. Nonlinear approximations of the dependencies of EnRs for (a) AAOD (388 nm) and (b) AOD (550 nm) on the photochemical age of BB aerosol. The dependencies are similar to those shown in Fig. 5a and 5b except that they are obtained without applying the correction involving CO columns (see Eqs. 2 and 3).

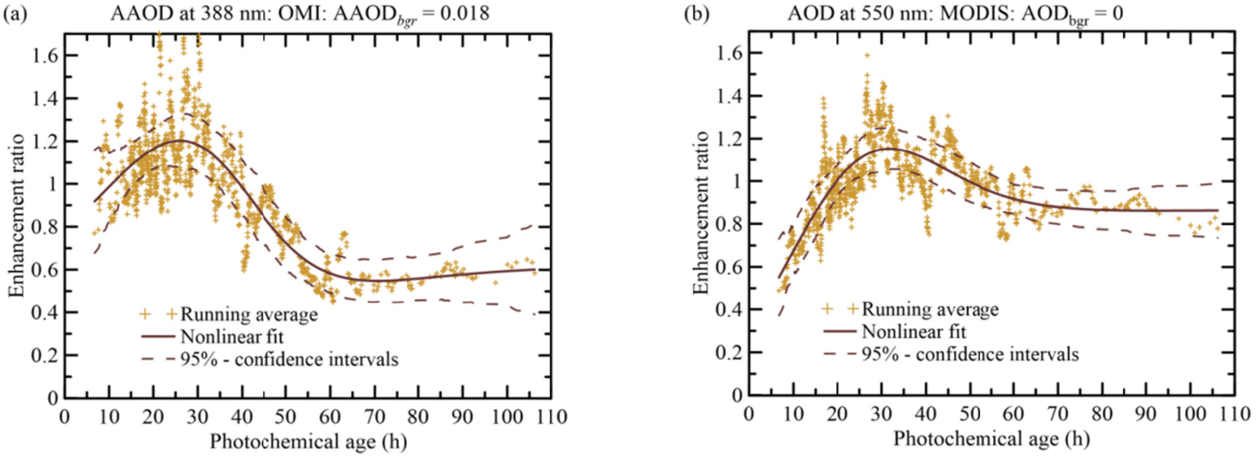

Figure S12. Nonlinear approximations of the dependencies of EnRs for (a) AAOD (388 nm) and (b) AOD (550 nm) on the photochemical age of BB aerosol. The dependencies are similar to those shown in Fig. 5a and 5b except that they are obtained assuming that the background AAOD ($AAOD_{bgr}$) equals to 0.018 and that the background AOD (AOD_{bgr}) equals to zero, respectively.

References

Ciarelli, G., El Haddad, I., Bruns, E., Aksoyoglu, S., Möhler, O., Baltensperger, U., and Prévôt, A. S. H.: Constraining a hybrid volatility basis-set model for aging of wood-burning emissions using smog chamber experiments: a box-model study based on the VBS scheme of the CAMx model (v5.40), Geosci. Model Dev., 10, 2303-2320, https://doi.org/10.5194/gmd-10-2303-2017, 2017.

Di Lorenzo, R. A., Washenfelder, R. A., Attwood, A. R., Guo, H., Xu, L., Ng, N. L., Weber, R. J., Baumann, K., Edgerton, E., and Young, C. J.: Molecular-size-separated brown carbon absorption for biomass-burning aerosol at multiple field sites, Environ. Sci. Technol., 51, 3128–3137, https://doi.org/10.1021/acs.est.6b06160, 2017.

Fleming, L. T., Lin, P., Roberts, J. M., Selimovic, V., Yokelson, R., Laskin, J., Laskin, A., and Nizkorodov, S. A.: Molecular composition and photochemical lifetimes of brown carbon chromophores in biomass burning organic aerosol, Atmos. Chem. Phys., 20, 1105–1129, https://doi.org/10.5194/acp-20-1105-2020, 2020.

Forrister, H., Liu, J., Scheuer, E., Dibb, J., Ziemba, L., Thornhill, K. L., Anderson, B., Diskin, G., Perring, A. E., Schwarz, J. P., Campuzano-Jost, P., Day, D. A., Palm, B. B., Jimenez, J. L., Nenes, A., and Weber, R. J.: Evolution of brown carbon in wildfire plumes, Geophys. Res. Lett., 42, 4623–4630, https://doi.org/10.1002/2015GL063897, 2015.

Konovalov, I. B., Beekmann, M., Berezin, E. V., Formenti, P., and Andreae, M. O.: Probing into the aging dynamics of biomass burning aerosol by using satellite measurements of aerosol optical depth and carbon monoxide, Atmos. Chem. Phys., 17, 4513-4537, https://doi.org/10.5194/acp-17-4513-2017, 2017.

Konovalov, I. B., Beekmann, M., Golovushkin, N. A., and Andreae, M. O.: Nonlinear behavior of organic aerosol in biomass burning plumes: a microphysical model analysis, Atmos. Chem. Phys., 19, 12091–12119, https://doi.org/10.5194/acp-19-12091-2019, 2019.

Luo, J., Zhang, Y., Wang, F., and Zhang, Q.: Effects of brown coatings on the absorption enhancement of black carbon: a numerical investigation, Atmos. Chem. Phys., 18, 16897–16914, https://doi.org/10.5194/acp-18-16897-2018, 2018.

Paris, J.-D., Stohl, A., Nédélec, P., Arshinov, M. Yu., Panchenko, M. V., Shmargunov, V. P., Law, K. S., Belan, B. D., and Ciais, P.: Wildfire smoke in the Siberian Arctic in summer: source characterization and plume evolution from airborne measurements, Atmos. Chem. Phys., 9, 9315–9327, https://doi.org/10.5194/acp-9-9315-2009, 2009.

Pokhrel, R. P., Beamesderfer, E. R., Wagner, N. L., Langridge, J. M., Lack, D. A., Jayarathne, T., Stone, E. A., Stockwell, C. E., Yokelson, R. J., and Murphy, S. M.: Relative importance of black carbon, brown carbon, and absorption enhancement from clear coatings in biomass burning emissions, Atmos. Chem. Phys., 17, 5063–5078, https://doi.org/10.5194/acp-17-5063-2017, 2017.

Sakamoto, K. M., Allan, J. D. Coe, H., Taylor, J. W., Duck, T. J., and Pierce, J. R.: Aged boreal biomass-burning aerosol size distributions from BORTAS 2011, Atmos. Chem. Phys., 15, 1633-1646, https://doi.org/10.5194/acp-15-1633-2015, 2015.

Selimovic, V., Yokelson, R. J., McMeeking, G. R., and Coefield, S.: In situ measurements of trace gases, PM, and aerosol optical properties during the 2017 NW US wildfire smoke event, Atmos. Chem. Phys., 19, 3905–3926, https://doi.org/10.5194/acp-19-3905-2019, 2019.

Sofiev, M., Ermakova, T., and Vankevich, R.: Evaluation of the smoke-injection height from wild-land fires using remote-sensing data, Atmos. Chem. Phys., 12, 1995–2006, https://doi.org/10.5194/acp-12-1995-2012, 2012.

Turquety, S., Hurtmans, D., Hadji-Lazaro, J., Coheur, P.-F., Clerbaux, C., Josset, D., and Tsamalis, C.: Tracking the emission and transport of pollution from wildfires using the IASI CO retrievals: analysis of the summer 2007 Greek fires, Atmos. Chem. Phys., 9, 4897–4913, https://doi.org/10.5194/acp-9-4897-2009, 2009.

Wong, J. P. S., Nenes, A., and Weber, R. J.: Changes in light absorptivity of molecular weight separated brown carbon due to photolytic aging, Environ. Sci. Technol., 51, 8414–8421, https://doi.org/10.1021/acs.est.7b01739, 2017.